Journal of Geophysical Research: Planets

RESEARCH ARTICLE
10.1029/2018JE005668

Unravelling the Mystery of Lunar Anomalous Craters Using Radar and Infrared Observations

Wenzhe Fa[1,2] **and Vincent R. Eke**[3]

[1]Institute of Remote Sensing and Geographical Information System, Peking University, Beijing, China, [2]Lunar and Planetary Science Laboratory, Macau University of Science and Technology, Macau, China, [3]Institute for Computational Cosmology, Department of Physics, Durham University, Durham, UK

Key Points:
- We constructed orthorectified global Mini-RF mosaics and analyzed anomalous craters in radar and infrared images
- Anomalous craters are not overabundant over the lunar polar regions once sampling variations are accounted for
- Anomalous craters actually represent an intermediate stage of normal crater evolution

Supporting Information:
- Supporting Information S1
- Data Set S1

Correspondence to:
W. Fa and V. R. Eke,
wzfa@pku.edu.cn;
v.r.eke@durham.ac.uk

Citation:
Fa, W., & Eke, V. R. (2018). Unravelling the mystery of lunar anomalous craters using radar and infrared observations. *Journal of Geophysical Research: Planets*, *123*, 2119–2137. https://doi.org/10.1029/2018JE005668

Received 4 MAY 2018
Accepted 28 JUN 2018
Accepted article online 5 JUL 2018
Published online 27 AUG 2018
Corrected 21 FEB 2019

This article was corrected on 21 FEB 2019. See the end of the full text for details.

Abstract In Miniature Radio Frequency (Mini-RF) radar images, anomalous craters are those having a high circular polarization ratio (CPR) in their interior but not exterior to their rims. Previous studies found that most CPR-anomalous craters contain permanently shadowed regions and that their population is overabundant in the polar regions. However, there is considerable controversy in the interpretation of these signals: Both water ice deposits and rocks/surface roughness have been proposed as the source of the elevated CPR values. To resolve this controversy, we have systematically analyzed >4,000 impact craters with diameters between 2.5 and 24 km in the Mini-RF radar image and Diviner rock abundance (RA) map. We first constructed two controlled orthorectified global mosaics using 6,818 tracks of Mini-RF raw data and then analyzed the correlations between radar CPR and surface slope, RA, and depth/diameter ratios of impact craters. Our results show that CPR-anomalous craters are distributed relatively uniformly across the lunar surface, with no apparent difference in CPR between the polar, potentially icy, and nonpolar, not icy, craters. Most CPR-anomalous craters are relatively young with a large depth/diameter ratio, and they actually represent an intermediate stage of crater evolution. Comparison with a two-component radar scattering model suggests that rocks and surface roughness are major contributors to the observed CPR values. Using craters of 4.7–22 km in diameter with known ages, we find that craters spend up to 120 Ma with a high exterior RA, and ~3 Ga in the CPR-anomalous phase.

Plain Language Summary Both rocky and icy surfaces look bright in radar images. Crater-producing impacts leave rocks strewn both inside and outside the resulting craters. These rocks are gradually reduced to dust by micrometeorite impacts and other weathering processes over many millions of years. Two recent Moon-orbiting imaging radars found a class of craters with radar-bright interiors that are radar dark on their outer slopes, named as anomalous craters. Also, more anomalous craters were found near the poles, where regions of permanent shade create regions cold enough for water ice to be stable. If rocks are broken down at the same rate inside and outside craters, then maybe these polar anomalous craters contain large ice deposits. We show that the large number of anomalous craters found near the poles is just a consequence of the imaging radars observing more of these parts of the lunar surface. The radar signals of well-observed craters do not vary with latitude. Rather than being hosts of ice deposits, anomalous craters are just an intermediate stage of crater evolution, with mass wasting down the steeper interior slopes refreshing the rocks for longer than it does on the shallower exterior slopes.

1. Introduction

Impact cratering is one of the most fundamental geological processes shaping the surface of an airless terrestrial body like the Moon. Cratering can shatter and fragment the crust, excavate materials from depth to the surface and transport them laterally, generate steep inner walls and form rugged ejecta blankets, produce regolith or megaregolith, and modify physical properties of the surface materials (e.g., Melosh, 1989). The major geological features produced by this process, impact craters, are the most dominant features on the Moon's surface. A newly formed crater is usually characterized by well-defined, sharp, and prominent features (e.g., slope, rim, and continuous ejecta) depending on projectile and target properties during the cratering process. Over time, a crater degrades and its characteristic features become less prominent as a result of impact erosion and other weathering processes (e.g., Fassett & Thomson, 2014; Ross, 1968). Consequently, the currently observed impact craters on the Moon exhibit a wide range of size- and age-dependent

morphologies. Understanding the formation mechanism and evolution of impact craters provides important clues about lunar chronology, the surface environment, the interior properties of the Moon, and the population of impactors in the early inner solar system.

Since 2007, a variety of state-of-the-art remote sensing instruments, operating in the γ-ray, ultraviolet, visible, infrared, microwave, and high-frequency band, with different principles and techniques, have been used to investigate the Moon. These instruments have returned a large quantity of data with unprecedented spatial resolution and quality, providing an opportunity to study impact craters from various aspects. For example, high-resolution optical images enable studies of the surface morphology, texture, and rocks associated with individual craters (e.g., Basilevsky et al., 2013; Speyerer et al., 2016) as well as more accurate surface age estimation from the crater size-frequency distribution (e.g., Morota et al., 2011). In contrast, infrared and microwave radiometer observations contain thermal information about the ejecta and regolith fines of impact craters (e.g., Bandfield et al., 2014; Ghent et al., 2016; Gong & Jin, 2013). Radar operating in the microwave band gives us a unique means to study impact craters from their surface down to a depth of several meters, because of its large penetration depth in the desiccated and porous regolith. In addition, radar has its own illumination, permitting the study of permanently shadowed craters where water ice could exist.

Impact craters over the lunar polar regions, if permanently shaded from direct sunlight, can act as cold traps where the physical temperature remains extremely low (for instance, mean temperature $\lesssim$50 K in ; Paige et al., 2010), allowing volatiles such as water ice to remain stable over geological timescales (e.g., Arnold, 1979; Lawrence, 2017; Lucey, 2009). Recent remote-sensing observations have provided multiple lines of evidence for the presence of lunar surface water (H_2O) and hydroxyl (OH^-) that could originate from solar wind implantation, impact delivery, and the interior of the Moon (e.g., Li & Milliken, 2017; Lucey et al., 2014; Pieters et al., 2009). However, these surficial deposits are not volumetrically significant from the viewpoint of resource usage. Therefore, the detection of a large quantity of water ice delivered by water-bearing debris or meteorites within the permanently shadowed regions (PSRs) near the lunar poles has been, and remains, a high-priority challenge in lunar science (for a review, the reader is referred to ; Lawrence, 2017). Recently, two orbital miniature synthetic aperture radars (India's Chandrayaan-1 Mini-SAR and NASA's Lunar Reconnaissance Orbiter (LRO) Miniature Radio Frequency [Mini-RF]) found a class of anomalous craters with high circular polarization ratio (CPR) only in their interior regions, but not exterior to their rims (Spudis et al., 2010; Spudis et al., 2013). Spudis et al. (2013) found that most of the anomalous craters they studied contained PSRs, and that anomalous craters were overabundant at the poles. Eke et al. (2009) applied image reconstruction techniques to neutron spectrometer data and inferred that hydrogen is typically concentrated into polar PSRs with a water ice equivalent concentration of up to $\sim$1 wt.%. These observations combined led Spudis et al. (2013) to interpret the anomalously high CPR regions as originating from water ice deposits. A rough estimation (the product of lateral extension of high interior CPR regions with a thickness of $\sim$10–20 m) suggested that the north polar region alone could contain 600 million metric tons of water ice (Spudis et al., 2013).

However, radar anomalous craters were also found over nonpolar regions, where water ice cannot be stable on the lunar surface because of the high temperature (e.g., Williams et al., 2017). Fa and Cai (2013) analyzed more than 70 impact craters (including both anomalous and fresh craters) across the lunar surface in Mini-RF images and quantified the influence of the surface slope, roughness, rock abundance (RA), dielectric permittivity, and regolith thickness on radar echo strength and CPR values. Their statistical analysis of CPR values showed that there is almost no apparent difference in radar CPRs between polar and nonpolar craters (both fresh and anomalous). Based on high-resolution optical images and a two-component mixture radar scattering model, they found that the high CPRs of nonpolar (and most probably polar) anomalous craters are caused by surface and subsurface rocks. Eke et al. (2014) reprocessed the Chandrayaan-1 Mini-SAR images with rectification of the parallax effect and analyzed the 42 impact craters in Spudis et al. (2010). Their results showed that the combined effect of parallax and incidence angle in unrectified radar images can bias the average interior CPR to larger values. Furthermore, they found no correlation between CPR and surface temperature, but high CPR regions tend to be located on the steep interior crater slopes. Based on all of these findings, Eke et al. (2014) concluded that high CPRs in polar anomalous craters are probably caused by factors such as surface roughness, and not the presence of water ice. To date, no consensus has been reached on the physical agent for the high CPR values associated with anomalous craters.

Meanwhile, Mini-RF images, in combination with auxiliary information about crater age, were used to investigate the physical properties and evolution of lunar impact craters. Eke et al. (2014) found that anomalous

craters have a depth/diameter ratio smaller than those of fresh craters, but larger than most polar craters (diameter range for all the studied craters: 2–20 km). This suggests that radar anomalous craters are of intermediate age. Ghent et al. (2016) investigated the physical properties of impact ejecta and their evolution for 24 craters with diameter between 18.6 and 99.6 km using radar (both Mini-RF and Arecibo) and Diviner thermal infrared observations. Using constraints from radar bright ejecta and dark haloes, they found that rocks within the upper meter of regolith can remain undisturbed by surface processes for over 3 Ga. According to the morphological age classification of impact craters in Pohn and Offield (1970), the 24 craters in Ghent et al. (2016) belong to Classes I ($\gtrsim$45 km in diameter) and II ($\sim$20–45 km in diameter). However, there is no systematic study of ejecta properties of smaller craters that fall into Class III ($\sim$8–20 km in diameter). Since the formation mechanism, morphology, and degradation of impact craters depend largely on crater size, investigating ejecta properties for small impact craters provides complementary information to that in Ghent et al. (2016). This will be of particular relevance for understanding polar radar anomalous craters, which typically belong to Class III.

In all previous studies, only a subset of impact craters over limited regions were investigated, provoking many important questions. For example, is there an overabundance of radar anomalous craters over the lunar polar regions? If so, then does it follow that water ice is producing the radar signal or are other factors responsible for the enhanced CPR within the interiors of anomalous craters? If radar anomalous craters are overabundant over the polar regions and if surface rocks are the physical agent for the elevated CPR values, then is this a sign that the low diurnal temperature variation in PSRs is decreasing the otherwise significant thermal fatigue of rocks? If rocks are driving the enhanced CPR, then why are rocks only present in the interiors of anomalous craters and what does this tell us about the weathering process affecting the lunar surface? Under what conditions is a crater fresh or anomalous? Can this inform us about the size-frequency distribution of rocks associated with impact craters at different degradation stages? One needs an exhaustive search of anomalous craters in global Mini-RF imagery and a systematic analysis of potential factors for elevated CPR in combination with other data sets to answer these questions.

In this study, we analyze more than 4,000 impact craters with diameters between 2.5 and 24 km in the LRO global Mini-RF image and Diviner RA map to resolve whether or not polar anomalous craters are overabundant and to quantify potential factors for elevated CPRs within anomalous craters. With our findings, we also combine fresh, anomalous, and old craters within the framework of normal crater evolution. This can inform us about how impact crater formation and evolution determines the distribution of surface and subsurface rocks both within a crater and in its ejecta. In addition, such a large population of impact craters enables us to investigate the role of target (maria versus highlands) in the formation and evolution of impact craters.

Section 2 contains a description of all the data sets used, along with details of how we constructed global orthorectified Mini-RF mosaics and found a set of 4,030 impact craters by applying an algorithm to a global digital elevation model (DEM) of the Moon. In section 3, we first answer the question whether or not polar anomalous craters are overabundant and then investigate the correlations between radar CPR, Diviner rock abundance, and depth/diameter ratio of impact craters. In section 4, potential factors for high CPR are investigated using a two-component mixture radar scattering model and the evolution of rocks associated with impact craters is discussed based on radar and infrared observations. Concluding remarks and remaining problems for future study are given in section 5.

2. Data Set and Crater Catalogue

In this study, we predominantly use the LRO Mini-RF data and Diviner RA data in our analysis of anomalous craters. The LRO Lunar Orbiter Laser Altimeter (LOLA) DEM is used for Mini-RF raw image rectification, crater finding, and crater depth/diameter determination. All of these data are available from NASA's Planetary Data System (PDS) Geosciences node (http://pds-geosciences.wustl.edu). This section describes the data and crater catalogues being used, and the data reduction procedures in the following analysis.

2.1. Mini-RF Global Mosaicking

The LRO Mini-RF system is a synthetic aperture radar (SAR) operating at S- (wavelength: 12.6 cm) and C-band (wavelength: 4.2 cm; note that this band is often incorrectly called as X-band). The nominal incidence angle is 49° $\pm$ 5°, and the spatial resolution is 150 m in baseline mode and 15 $\times$ 30 m (azimuthal $\times$ range) for zoom mode (Nozette et al., 2010). Mini-RF used a hybrid polarimetric architecture, that is, transmitting a left-hand circular polarized radar wave and receiving two orthogonal linear polarization (horizontal H and vertical V)

echoes simultaneously (e.g., Raney et al., 2011). The Stokes vector can be constructed from the two received linear polarization echoes, and then radar backscattering coefficients (e.g., σ_{oc} for the opposite-sense circular polarization and σ_{sc} for the same-sense circular polarization) and daughter products (e.g., CPR = σ_{sc}/σ_{oc}) can be calculated (Carter et al., 2011; Fa et al., 2011). In this study, we will focus only on S-band zoom data products because most previous studies of the spatial distribution of CPR-anomalous craters used only S-band data. In addition, Mini-RF C-band coverage is too sparse to give statistically significant results on the spatial distribution of CPR-anomalous craters (see Figures S1 and S2 in the supporting information for the coverage of Mini-RF observations). The Mini-RF accumulated in total ~ 67% coverage of the lunar surface for the S-band observations with a spatial resolution of 30 m, including ~ 99% coverage for the two polar regions (Cahill et al., 2014).

In many previous studies using Mini-RF observations (e.g., Cahill et al., 2014; Fa & Cai, 2013; Spudis et al., 2010; Spudis et al., 2013), the raw radar data were not rectified. SAR is designed to be side-looking and raw data are usually mapped into spatial coordinates by assuming a flat surface. Variations in lunar topography cause a radar parallax effect that is generally larger than the spatial resolution of Mini-RF, distorting the map of inferred radar echo locations. As an example, for a fresh crater with a diameter of 10 km and a depth of 2 km (corresponding to a depth/diameter ratio of 0.2), the parallax would be ~1.7 km (~58 pixels) for the crater center (based on equation 4.37 in Campbell, 2002). The combined effect of a side-looking instrument (e.g., SAR) and parallax, results in uneven sampling of the crater interior region, with the near walls occupying more than half of the crater area in an unrectified map. As the near walls are viewed at higher incidence angles and the CPR increases with increasing incidence angle, this will bias the interior CPR to a larger value if it is determined using an unrectified map (Eke et al., 2014). Analysis of the eight craters in Fa and Cai (2013) shows that the parallax effect can change CPR by up to 4% and make a ~20–60% difference in SC and OC (Table S1 in the supporting information). A case study for a crater of 6 km in diameter with a radar incidence angle of 33° (for Chandrayaan-1 Mini-SAR) shows that the combination of incidence angle and the parallax effect can increase the peak of the CPR distribution from 0.65 to 0.8 from the exterior to the interior of the crater (see Figure 9 in Eke et al., 2014). Therefore, rectification of Mini-RF raw data using high resolution topography data is a prerequisite for a statistically fair result (e.g., Eke et al., 2014; Thomson et al., 2012).

In this study, Mini-RF level 1 raw data are used. These are radar signals after range and azimuth compressions, and their pixel coordinates are not georeferenced. In signal processing of the zoom mode, the spatial resolution is chosen as 7.5 m/pixel to ensure the intrinsic resolution of the instrument is oversampled. The hybrid polarimetric architecture of Mini-RF means that each level 1 pixel has four observed values (or four channels): the horizontal polarized intensity, the vertical polarized intensity, and the real and imaginary parts of the cross-product between H and V polarizations. We processed 6,818 tracks of Mini-RF level 1 raw data according to the main procedures in Kirk et al. (2010) by using the USGS Integrated Software for Imagers and Spectrometers version 3 (ISIS 3). The level 1 data were first imported into ISIS using the program *mrf2isis* and were then assigned corresponding trajectory data from the SPICE SPK file using the program *spiceinit*. Each individual image was orthorectified with the program *cam2map* using a LOLA DEM with a spatial resolution of 128 pixels/degree. In these three steps, the four channels of each level 1 track were processed individually, and the output is the orthorectified Stokes vector. The Stokes vector is further used to calculate the orthorectified same- and opposite-sense circular backscattering coefficients (σ_{sc} and σ_{oc}), and then the orthorectified CPR value (CPR = σ_{sc}/σ_{oc}). Finally, all of the individual orthorectified images were mosaicked using the program *automos* with a given projection type.

In the mosaicking, the polar stereographic projection is used for both the north (latitude > 70°N) and south (latitude < 70°S) poles, and the equirectangular projection is used for the nonpolar regions (|latitude| < 70°). Level 1 data were downsampled to a spatial resolution of 100 m/pixel to be comparable with other data sets and to reduce data volume. As the Mini-RF system has both east- and west-looking directions and the radar echo depends significantly on incidence angle (e.g., Fa et al., 2011), we split the data into two groups based on look direction. We made two controlled global CPR mosaics with east- and west-looking directions, with a spatial resolution of 100 m/pixel. As an example, Figure 1 shows the east-looking global CPR mosaic. The west-looking global CPR mosaic is given in Figure S3. From Figure 1, coverage of Mini-RF data for the polar regions is much larger than that of the nonpolar regions, and hence, craters near the two poles are well-sampled by Mini-RF. Therefore, for a fair comparison of crater numbers between the polar and nonpolar regions, the difference in Mini-RF coverage should be considered.

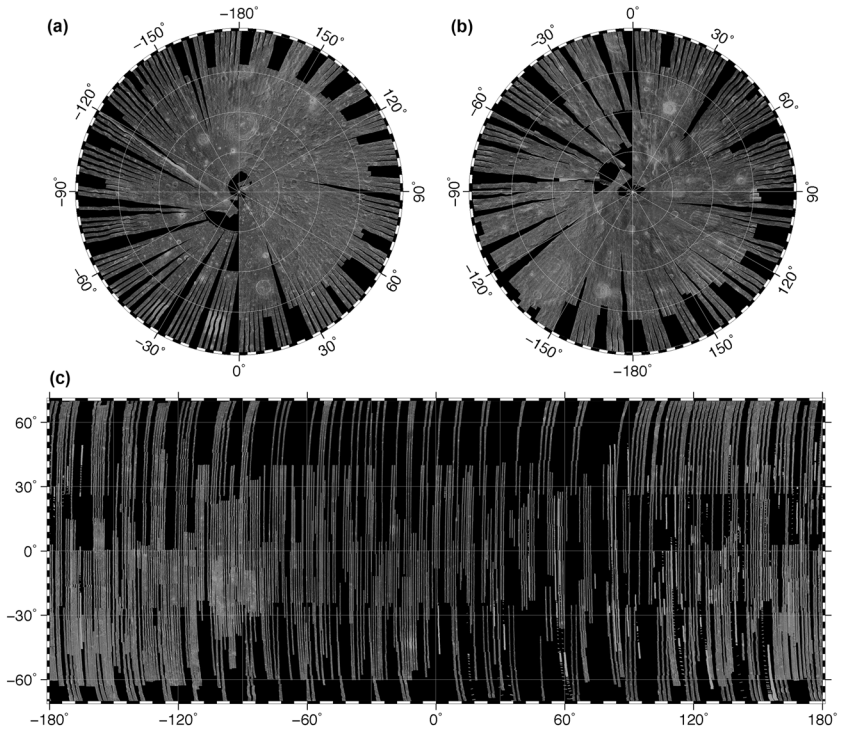

Figure 1. Global mosaic of the Mini-RF east-looking CPR map. (a) The north pole from 70°N and (b) the south pole from 70°S, both in the polar stereographic projection. (c) Cylindrical projection of the nonpolar region with latitudes from 70°S to 70°N. Brighter tones indicate higher CPR values. The spatial resolution is 100 m/pixel.

2.2. Diviner RA Data

The difference in the thermal inertia of rocks and fine-grained regolith causes a temperature difference between rock and regolith during lunar nighttime. This provides a means to estimate rock abundance from multispectral thermal infrared observations. Based on this principle, the areal fraction of surface rocks with size $\gtrsim$1 m, defined as the rock abundance, RA, was estimated using Diviner nighttime brightness temperatures at 13–23, 25–41, and 50–100 μm by Bandfield et al. (2011). In deriving RA values, local slopes were taken into account with respect to modeled temperatures of surface rocks. We use RA values derived from Diviner observations collected from 5 July 2009 to September 2012. The coverage of the RA data is from 80°S to 80°N, and the spatial resolution is 128 pixels/degree, corresponding to ~236.9 m/pixel at the lunar equator. Away from craters, the background RA value is typically only ~0.004–0.006, with a standard deviation of <0.0015 that can be taken as an indicator of the RA precision. Maria surfaces show slightly higher RA because of the many rocks associated with numerous small impact craters. In contrast, small craters in the highlands do not typically have rocks and only larger craters, with diameters greater than several kilometers, show elevated RA. Due to shadowing at high latitudes, the diurnal temperature range is too low to yield a reliable estimate of the RA. Consequently, the coverage of the RA map decreases progressively for regions with |latitude| $\geq$ 60°.

2.3. Impact Crater Catalogue

We use the automated crater-finding algorithm described by Eke et al. (2017) to find impact craters in the global lunar topographical data. This algorithm simulates the gradual flooding of the topography with virtual water, and crater candidates are found by looking for near-circular virtual puddles. LOLA topographical data in the cylindrical projection with a spatial resolution of 128 pixels/degree are used for the region with |latitude| < 75°, and those in the polar stereographic projection with a resolution of ~240 m/pixel are used for the two poles. An initial search results in >115000 candidate craters with diameters between 2.5 and 24 km. The abundance of craters is within 10% of that in the Lunar Crater Catalogue LU78287GT from Salamunićcar et al. (2014) at all diameters from 30 km up to 100 km, where the results are also similar with those from Head et al. (2010). This, along with detailed checks in small areas, gives us confidence to extrapolate to smaller craters using our catalogue. We put in several additional criteria to find well-defined craters, including that the rim is a local maximum in elevation, that the elevation drops off smoothly to 1.5r_c (r_c: crater radius), and that

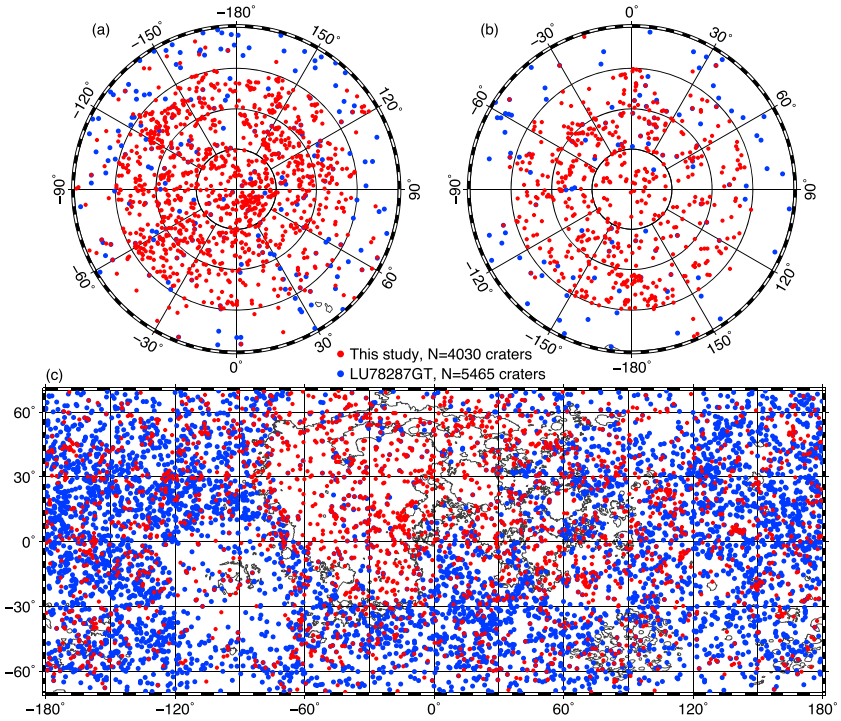

Figure 2. Global distribution of the 5465 craters (blue) with diameters between 8 and 20 km from the LU78287GT catalogue and the 4,030 craters (red) with diameters between 2.5 to 24 km. (a) The north pole from 70°N and (b) the south pole from 70°S, both in the polar stereographic projection. (c) Cylindrical projection of the latitudes from 70°S to 70°N. The black curves outline the boundary of the mare basalts from the USGS (Laneuville et al., 2013).

the elevation increases approximately monotonically from $0.5r_c$ to r_c, with $0.5r_c$ being higher than the crater center. With these additional criteria, 4,030 impact craters with diameters between 2.5 and 24 km were found in total, of which 1,099 craters are located over the north pole (> 70°N), 536 craters are located over the south pole (<70°S), and 2,395 craters are located in nonpolar regions (|latitude| < 70°).

The above algorithm and rules tend to select craters with larger depth/diameter ratios. Thus, this database of small craters cannot be used to determine crater number densities because it has uncertain completeness. We use the LU78287GT catalogue to provide a set of craters with diameters > 8 km that samples the lunar surface more uniformly than the set of 4,030 from our own catalogue. This crater catalogue contains 78,287 impact craters and is claimed to be complete for craters with diameters >8 km. In our analysis below concerning with crater number density, we also selected the 5,465 impact craters with diameters between 8 and 20 km from the LU78287GT crater catalogue.

Figure 2 shows the distributions of all the craters in these two catalogues. Craters with diameters between 2.5 and 24 km are distributed relatively uniformly across the low-latitude regions. In contrast, most craters with diameter >8 km in LU78287GT are concentrated into the lunar highlands. This reflects the older age of the highlands relative to the maria. Compared with nonpolar regions, the two polar regions have more abundant small impact craters (<8 km), but this just reflects the spatially variable completeness in our catalogue.

2.4. Registration of the Data Sets

As LRO Mini-RF, Diviner, and LOLA all use the same spacecraft position information, coregistration between these data sets should not be a significant problem at the spatial resolution (~100 m) in our analysis. However, offsets between the locations of craters in the LOLA DEM and Mini-RF are evident (as an example, see Figure 1 in Fa and Cai (2013)). We have estimated the size of this effect empirically using the 2900, out of 4030, craters with a difference of at least 0.1 between their median interior and exterior CPR pixel values. This distinction is sharp enough that these craters can be used to determine the typical shift required to coregister the Mini-RF and LOLA maps. The median shift required is ~0.9 km, which is significantly smaller than the typical crater size we are studying. Consequently, the rectification of the Mini-RF map should not be too inappropriate as a result of the misregistration that is present in the PDS data sets.

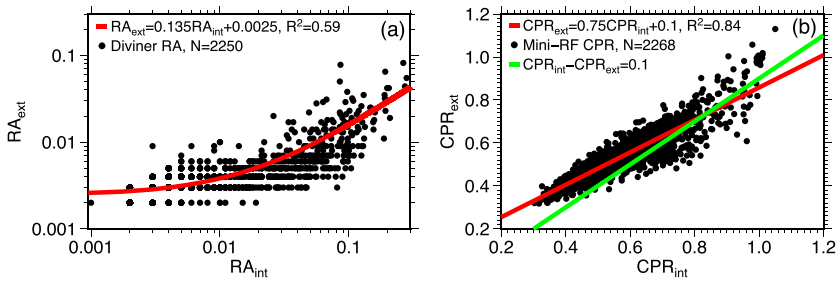

Figure 3. (a) Exterior (out to $1.4r_c$) RA versus interior RA and (b) Exterior CPR versus interior CPR for all the well-sampled craters in the 4030 crater catalogue. The black dots represent median values for the interior and exterior regions. The red lines represent the best fit linear relations in both cases. The green line represents the interior and exterior median CPR difference of 0.1, and craters on the right of this line are CPR anomalous. CPR = circular polarization ratio; RA = rock abundance.

3. Results

This section is split into three main parts, the first of which shows general relations between interior and exterior regions for RA and CPR. The second part addresses the relative abundance of anomalous craters at different latitudes and its implication for water ice. The third part considers what the existence of anomalous craters can teach us about the process of crater evolution.

3.1. General Relation Between Crater Interior and Exterior Regions

In the analysis below, distributions of surface topography, slope, CPR, and RA are associated with each crater. We will emphasize the differences in these properties between crater interior and exterior regions. For each crater, the study region goes from the crater center to 1.4 times the crater radius. This choice of outer boundary makes the surface areas of the interior and exterior regions approximately equal so that noise properties are similar. Since lunar surface CPR and RA distributions are generally non-Gaussian with long tails (e.g., Bandfield et al., 2011; Fa & Cai, 2013), their median values are used as a more robust measure than the mean pixel value.

We only consider well-sampled craters with data coverage larger than 90%. For the 4,030 crater catalogue, in total, there are 2,250 well-sampled craters in the RA map, and 2,268 well-sampled craters by Mini-RF. When a crater is well-sampled by Mini-RF in both west- and east-looking mosaics, we take the mean of the two median pixel CPR values. Figure 3 shows the relations between crater interior and exterior median values of RA and CPR. A linear relation exists for both RA and CPR, with $RA_{ext} = 0.135RA_{int} + 0.0025$ and $CPR_{ext} = 0.75CPR_{int} + 0.10$. 50% of craters have $RA_{int} > RA_{ext}$, and 43% have equal interior and exterior values (the RA values are discretized to 0.001, as is evident in Figure 3). For CPR, 74% of craters have larger interior values, with the CPR difference varying from 0 to 0.35, whereas the remaining 26% having interior CPR values that are less than 0.1 smaller than those in the exterior regions. In general, fresh craters possess large CPR and RA in both interior and exterior regions, and old craters have small CPR and RA values. Similar results are found for all the well-sampled craters with diameters of 8–20 km in the LU78287GT catalogue, and details are given in Figure S4.

3.2. Spatial Distribution of CPR-Anomalous Craters

To study the distribution of radar anomalous craters in the CPR maps, we define CPR-anomalous craters as those with $\Delta CPR = CPR_{int} - CPR_{ext} \geq 0.1$. While there is disagreement in the literature as to the cause of CPR-anomalous craters, the issue we seek to address here is how uniformly distributed they are over the lunar surface. Figure 4 shows the spatial distribution of CPR-anomalous craters for both our sample and the subset of LU78287GT craters with diameters of 8–20 km. Relative to the LU78287GT subsample, our anomalous craters are concentrated towards the poles. However, this merely reflects the uneven coverage that was already illustrated in Figure 2.

3.2.1. Are Polar Radar Anomalous Craters Overabundant?

With the distribution of CPR-anomalous craters in Figure 4, it is now possible to quantify whether or not polar radar anomalous craters are overabundant. Figure 5 shows the number density of craters as a function of latitude for all LU78287GT craters with diameters of 8–20 km, the subset of those that are well-sampled with Mini-RF data, and the number density of craters that are both well-sampled and CPR-anomalous. We use the LU78287GT craters to determine these number densities because this catalogue is more complete (Salamunićcar et al., 2014).

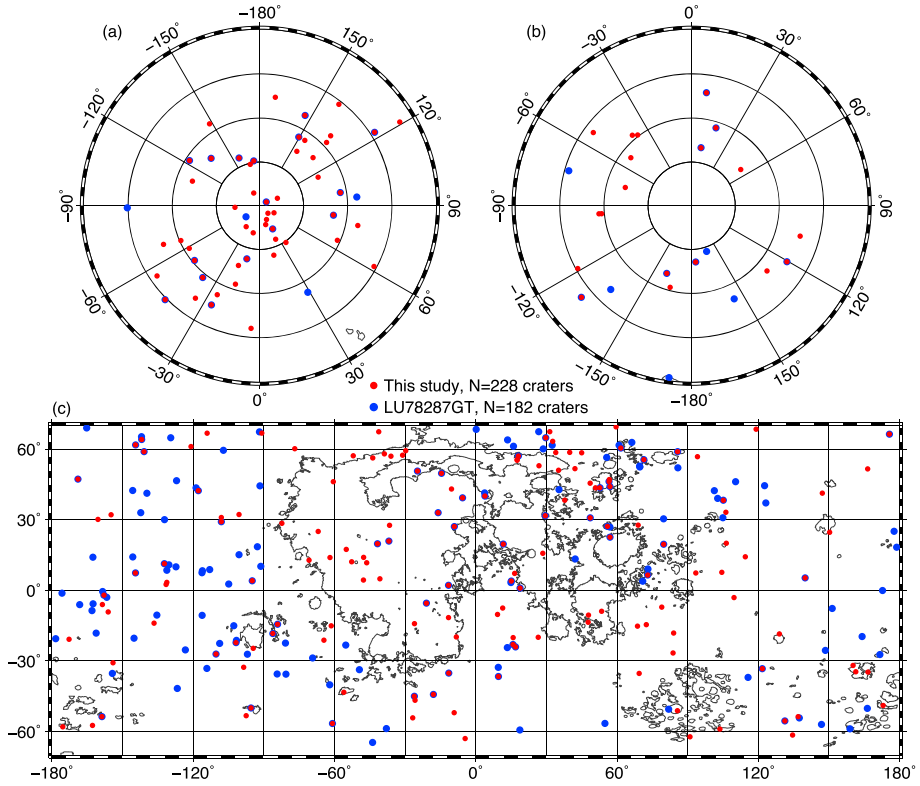

Figure 4. Global distribution of the 228 (red) CPR-anomalous craters in the 4,030 crater catalogue and the 182 (blue) CPR-anomalous craters in the LU78287GT catalogue. (a) The north pole from 70°N and (b) the south pole from 70°S, both in the polar stereographic projection. (c) Cylindrical projection of the latitudes from 70°S to 70°N. The black curves outline the boundary of the mare basalts from the USGS (Laneuville et al., 2013). CPR = circular polarization ratio.

From Figure 5a, the number density of craters with diameters of 8–20 km varies slightly with latitude, having a maximum at mid-high latitudes of 45°–65° . This is consistent with the relative cratering rate on the Moon in Le Feuvre and Wieczorek (2011), which predicts only a 20% variation in cratering rate for impact craters with diameter > 1 km across the lunar surface. However, because of the high-priority for Mini-RF observations over the polar regions, the number density of radar well-sampled craters increases significantly away from the equator. As a consequence, the number density of craters that are both well-sampled and CPR-anomalous is about 7–8 times higher in the polar regions at |latitude| > 80° than it is in the equatorial regions. Nevertheless, the fraction of well-sampled craters that are CPR-anomalous shows no significant evidence that polar CPR-anomalous craters are overabundant, as shown in Figure 5b. A constant anomalous fraction of 0.17, independent of latitude, represents a good fit to the measurements. The two lunar poles are typical highland terrain, whereas the nonpolar regions consist of maria and highlands. To exclude the geological target effect on the spatial distribution of CPR-anomalous craters, Figures 5c and d show the areal density and the ratio of CPR-anomalous craters as a function of latitude for highlands craters only. Once again, there is no significant evidence that polar CPR-anomalous craters are overabundant.

The overabundance of polar CPR-anomalous craters found by Spudis et al. (2013) is most probably caused by the fact that the polar regions are more likely to have been observed by Mini-RF than nonpolar regions (99% versus 67%), making it easier to find polar anomalous craters. A similar test can be performed using craters with diameter < 8 km from our 4030-crater sample, by determining the fraction of radar-well-sampled craters that are CPR-anomalous as a function of latitude. Again, this exercise shows no significant overabundance of CPR-anomalous craters at the poles (details are in Text S1).

In our Mini-RF image mosaicking, an equirectangular projection is used for the nonpolar region (|Latitude| < 70°), and polar stereographic projections are used for the two poles (|Latitude| > 70°). The equirectangular projection can cause distortion at mid to high latitudes. However, this does not affect any of our results, because we only consider well-sampled craters (Mini-RF coverage >90%) and account for the differing areas

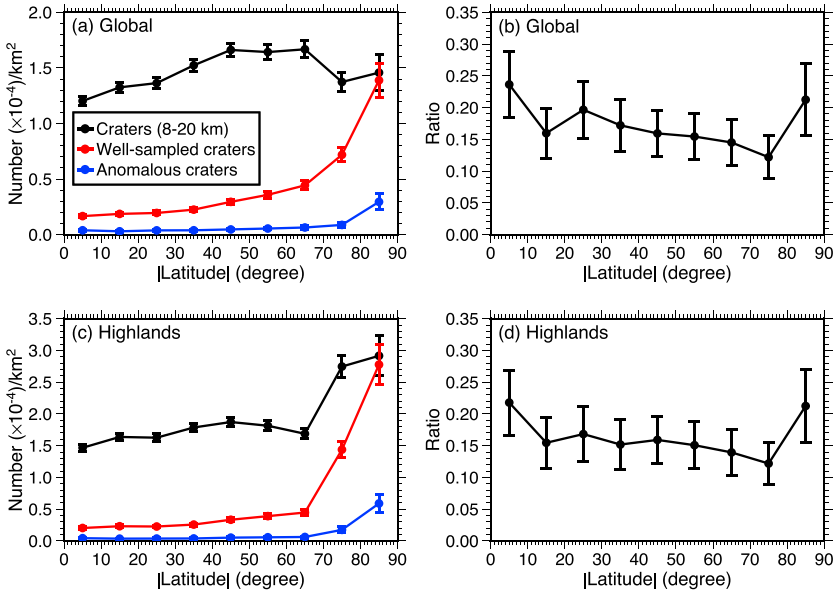

Figure 5. (a) Areal density of LU78287GT craters with: 8 ≤ diameter/km ≤ 20 (black), the subset with Miniature Radio Frequency (Mini-RF) coverage ≥ 0.9 (red), and the subset with Mini-RF coverage ≥ 0.9 and ΔCPR ≥ 0.1 (blue). (b) Fraction of well-sampled craters that are CPR-anomalous as a function of latitude, folding together both hemispheres. (c) Areal density of LU78287GT craters over the highlands with: 8 ≤ diameter/km ≤ 20 (black), the subset with Mini-RF coverage ≥ 0.9 (red), and the subset with Mini-RF coverage ≥ 0.9 and ΔCPR ≥ 0.1 (blue). (d) Fraction of well-sampled craters over the highlands that are CPR-anomalous as a function of latitude, folding together both hemispheres. The error bars in (a) and (c) represent 1σ statistical uncertainties assuming a Poisson distribution, and the error bars in (b) and (d) follow from the straightforward propagation of errors.

of each pixel being used when calculating median pixel CPR values. Also, the pixel areas do not vary much within the vast majority of our craters, because they all have diameters smaller than 24 km. For example, in the 4,030 crater catalogue, there are only five craters that cross the ±70° lines where the craters go from cylindrical to polar stereographic projections. In these cases the ratio of maximum/minimum pixel areas is 2.7. For the other 4,025 craters, this ratio is <1.08, that is, the largest pixel is <8% larger than the smallest one.

3.2.2. Implications for Water Ice over the Lunar Polar Regions

At the moment, there is no direct means systematically to obtain the abundance of surface rocks over the lunar polar regions directly from remote sensing observations. The Lunar Reconnaissance Orbiter Camera (LROC) Narrow Angle Cameras (NACs) conducted long-exposure observations over a certain number of PSR craters using the diffuse sunlight reflected from crater walls and nearby massifs around the solstice (Koeber et al., 2014; Mitchell et al., 2017). Preliminary results revealed that some PSR craters (e.g., Kocher, Sylvester N) do contain abundant exposed rocks with sizes from 20 to 50 m, but have no detected reflective anomaly (a signature of water frost). In future, as all the PSRs are imaged at a high spatial resolution, one needs to examine those CPR-anomalous craters without surface rocks, which could be potential sites for water ice deposits. Nevertheless, even if polar CPR-anomalous craters were found with no interior surface rocks, there would still be no means to exclude the possibility of the CPR signal resulting from subsurface rocks (Fa & Cai, 2013). Furthermore, neutron spectroscopy measurements rule out deposits of ≳10 wt.% water ice within the upper meter of the Moon that are at least O(10 km) in size (e.g., Lawrence et al., 2011).

Bistatic radar can provide measurements of radar echo as a function of bistatic (phase) angle, which can be used to search for the coherent backscatter opposition effect (CBOE) that is indicative of the presence of a weakly absorbing medium (e.g., pure water ice or regolith; e.g., Hapke, 1990; Peters, 1992). The recent Mini-RF bistatic experiment reported a CBOE-like CPR peak at small phase angle on the floor of Cabeus crater, which is different from the observed opposition responses from the ejecta of several Copernican-aged craters (Patterson et al., 2017). This unique opposition surge at Cabeus is interpreted as possible evidence for near surface deposits of water ice. While the phase angles of these bistatic campaign are similar, the radar incidence angle on the floor of Cabeus is much larger than those of the Copernican-aged craters (82.4–86.8° versus 41–71° , Tables 2 and 3 in Patterson et al., 2017). Previous studies show that CPR increases with radar incidence angle,

and CPR at an incidence angle of 80° is ~2–3 times larger than that at 40° (e.g., Fa et al., 2011; Thompson et al., 2011). Therefore, the CBOE-like CPR peak over Cabeus may result from the large radar incidence angle. To exclude this possibility, future Mini-RF bistatic observations should compare different geological targets with the same viewing geometry. Also, the occurrence of CBOE due to volume scattering only indicates the presence of a weakly absorbing medium (e.g., Hapke, 1990). Pure water ice is not the only such weakly absorbing material. Other materials, such as sulfur and regolith with low ilmenite abundance, are weakly absorbing as well. Therefore, CBOE alone is not a diagnostic signal for the presence of water ice.

Note that our results exclude the presence of a large quantity of pure water ice over large regions near the lunar poles. However, our results do not preclude the existence of a few percent of water ice that fills the pores in the regolith. If there is only a small percent of water ice, or if there is a veneer of water frost with a thickness much smaller than radar wavelength (Lucey et al., 2014), then the effective dielectric permittivity of the regolith-ice mixture will differ so slightly from that of typical regolith (see Figure 16 in Fa et al., 2011) that Mini-RF will not be able to detect its effect on the CPR. This has been verified by both theoretical modeling (Fa et al., 2011) and Mini-RF observation of the LCROSS impact site (Neish et al., 2011), where the concentration of water ice is estimated to be 5.6±2.9 wt.% (Colaprete et al., 2010).

In our study, we only analyzed Mini-RF S-band data. There are also C-band observations, though the data coverage (Figure S1) is very sparse. Combined analysis of S- and C-band data products could provide information from the surface and subsurface to a depth of several meters. For example, C-band observations are sensitive to surface roughness and smaller rocks ($\lesssim$cm), but cannot see subsurface scatterers several meters deep. The Mini-RF S-band can see at least several meters, and therefore provides information on subsurface inhomogeneity. To provide quantitative information about the subsurface, one needs to study radar echo behavior as a function of radar wavelength. In addition, surface roughness is scale dependent and one needs to quantify how roughness differs at the two wavelengths. Using dual-frequency data could be a method for water ice detection, but more work on scale-dependent scattering modeling and better understanding of surface properties would be prerequisites for such studies.

3.3. Evolution of Impact Craters

Given that the CPR-anomalous craters are present across the lunar surface, with no intrinsic preference for polar locations, one is led to wonder what has given rise to such craters. In this subsection, we present results that suggest these craters are just part of the normal evolutionary sequence for lunar impact craters.

3.3.1. Variation with Crater Depth/Diameter Ratio

As a crater degrades, it becomes shallower and its diameter increases due to the cumulative effect of micrometeorite bombardments (e.g., Fassett & Thomson, 2014). Therefore, the depth/diameter ratio of a crater can be used as a measure of its relative age, with a larger value indicating a younger crater. Figures 6a and 6b show the differences in CPR and RA between the crater interior and exterior regions as a function of depth/diameter ratio for all of our well-sampled craters with diameters between 2.5 and 24 km. One can see that ΔCPR (=CPR_{int} − CPR_{ext}) and ΔRA (=RA_{int} − RA_{ext}) increase with depth/diameter ratio, especially when the depth/diameter ratio is larger than ~0.1.

The crater degradation state, as indicated by the depth/diameter ratio, also depends on diameter. To highlight the behavior of ΔCPR as a function of crater degradation state, it is better to use a narrower diameter range of craters while keeping the diversity of degradation state. As the population of larger craters is generally small, we selected impact craters with diameters of 3–4 km for detailed study. Figure 6c shows ΔCPR as a function of depth/diameter ratio for these smaller craters. In contrast with the behavior in Figure 6a, ΔCPR peaks at a depth/diameter of ~0.17 and decreases at higher depth/diameter. Given the uncertainty in coregistration between the Mini-RF image with topography data, we further shifted the center of each crater to obtain the maximum ΔCPR. During shifting, the maximum difference in distance between the centers of the unshifted and shifted CPR maps is set to 1.4 km. Figure 6d shows ΔCPR as a function of depth/diameter for the shifted craters. The variation is more evident in Figure 6d because anomalous craters, which tend to have depth/diameter ~0.15, preferentially have their ΔCPR increased during the shifting of the CPR map. Note that after shifting, the depth/diameter ratio at which ΔCPR is the largest decreases from ~0.17 to ~0.15.

The same shifting algorithm can be applied to all the well-sampled craters in Figure 5, and an alternative result (Figure S5) for the latitude dependence of CPR-anomalous craters can be obtained. Once again, there is no significant evidence for a latitude dependence in the fraction of CPR-anomalous craters (ΔCPR $\geq$ 0.1).

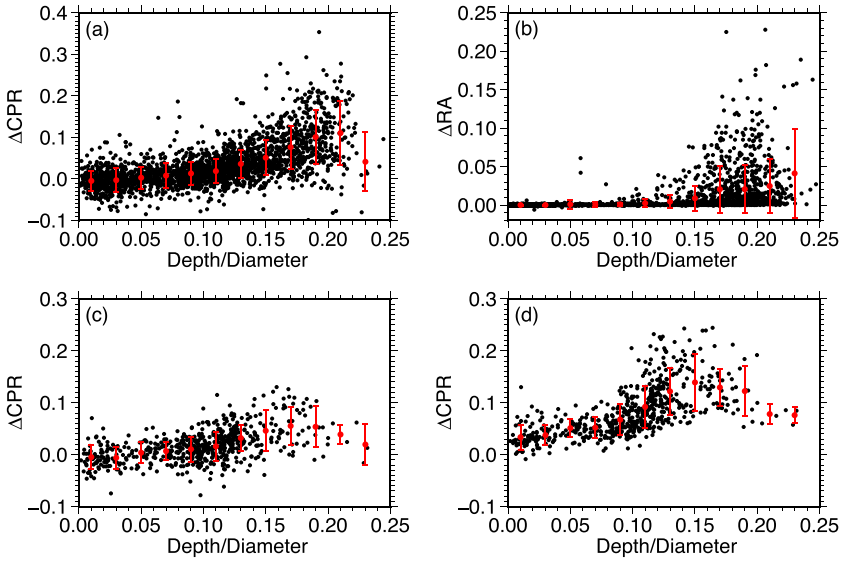

Figure 6. Difference in circular polarization ratio (a) and rock abundance (b) between crater interior and exterior regions as a function of crater depth/diameter ratio for all of our well-sampled impact craters. Black dots are for individual craters, and red dots are average values within depth/diameter bins of width 0.02, with the error bars indicating the 68% confidence interval on the means assuming that the individual crater values in each bin are Gaussian distributed. Panels (c) and (d) are just for craters with diameters between 3 and 4 km and represent results respectively without and with a shift of the circular polarization ratio map to try and align it with the Lunar Orbiter Laser Altimeter digital elevation model.

We found that a constant fraction of 0.25, rather than the 0.17 from before the shift was applied, provides a good fit.

The dependence of ΔCPR and ΔRA on depth/diameter ratio in Figure 6 reflects the evolution of impact craters. In CPR and RA images, young fresh craters with a large depth/diameter ratio usually have comparably high CPR and RA values in both their interior and exterior regions, whereas old craters with a smaller depth/diameter ratio are characterized by low CPR and RA values. Anomalous craters can be regarded as an intermediate class, where the interior CPR and RA values are larger than the corresponding values in the exterior region. This can explain the variation of ΔCPR as a function of depth/diameter ratio in Figures 6c and d. Note that there is no clear drop in ΔRA at larger depth/diameter ratio like that seen in ΔCPR. This may imply that the exterior RA is smaller than that of the interior region upon crater formation, or it may be that too few sufficiently young craters exist in our sample to show this trend.

3.3.2. Case Studies of Individual Craters

As the crater degradation state evolves, the crater interior and exterior CPR and RA generally decrease. To study the evolution of impact craters and to investigate the behavior of craters in the optical, radar, and infrared RA maps, we selected five impact craters (labeled as craters 1–5, Table 1 and Figure 7) for detailed analysis. These five craters are located over the highlands and their diameters vary from ~7 to 10 km. These two selection criteria can help to minimize the effect of geological target and diameter on the formation and degradation of impact craters.

In optical images, crater 1 has a sharp, well-defined crater rim, and its exterior region is characterized by "elephant hide" slope textures or regolith ripples (Melosh, 2011; Xiao et al., 2013) that extend more than two diameters from the rim. Abundant rocks with diameters from several to tens of meters can be found in its interior and exterior regions. Craters 2–4 have well-defined rims, but they are not as sharp as that of crater 1. Faint "elephant hide" slope textures can be found in the exterior regions of craters 2 and 3, but not for crater 4. Sporadic rocks with diameters from several to tens of meters exist on the exterior slopes of crater 2, but no meter-scale rocks can be found in the exterior regions of craters 3 and 4. The rim and the interior region of crater 5 are flatter than those of the corresponding regions of craters 1–4. The diameter and number of impact craters superposed on the exterior regions of their rims increase sequentially from craters 1 to 5. All of these morphological characteristics indicate that these five craters become older from craters 1 to 5.

Table 1
Information for the Five Impact Craters Used as Case Studies

				CPR		RA	
Crater	Location	Diameter (km)	Depth/diameter	Interior	Exterior	Interior	Exterior
1	30.49° N, 84.02° E	8.4	0.22	0.96	0.91	0.034	0.017
2	37.92° S, 156.67° W	7.3	0.19	0.92	0.85	0.012	0.004
3	44.05° N, 57° E	9.4	0.21	0.78	0.54	0.015	0.002
4	30.94° N, 108.08° W	7.5	0.19	0.72	0.60	0.005	0.004
5	39.55° N, 71.12° E	8.1	0.07	0.51	0.52	0.004	0.004

Note. CPR = circular polarization ratio; RA = rock abundance.

Figure 8 shows the surface elevation normalized by crater diameter, bidirectional slope, CPR and RA for these five impact craters. From left to right, craters become shallower and the inner wall slope decreases. For craters 1 and 2, the interior and exterior CPRs are high and comparable. The interior CPR values of craters 3 and 4 are much larger than their exterior ones, the signature of CPR-anomalous craters. For crater 5, the interior and exterior CPR are roughly equivalent, and both are low. Note that the high sporadic CPRs near the rim are contamination by small fresh craters.

In the RA map, crater 1 has both high interior and exterior RA, though the interior RA is about twice that of the exterior region. Craters 2 and 3 have much higher interior RA values, and low exterior RA values that are equivalent to the background value. For craters 4 and 5, RA values in both the interior and exterior regions are similarly low.

Moving from left to right in Figure 8, it is apparent that exterior RA or CPR values can be low while the corresponding values for the interiors of the craters are high. Furthermore, using the evolutionary order implied by the optical images, it is possible to infer that the exterior values of these properties decrease more rapidly than those for the crater interiors, and that both interior and exterior RA values decrease more quickly than the corresponding CPR values. As Mini-RF CPR is sensitive to rocks from the surface to a depth of a few meters, this implies that surface rocks are weathered away more rapidly than subsurface rocks.

Figure 9 shows the radial profiles for the normalized surface elevation, surface slope, CPR and RA for these five craters. Depth/diameter ratios of the first four craters are large and very similar, while the depth/diameter

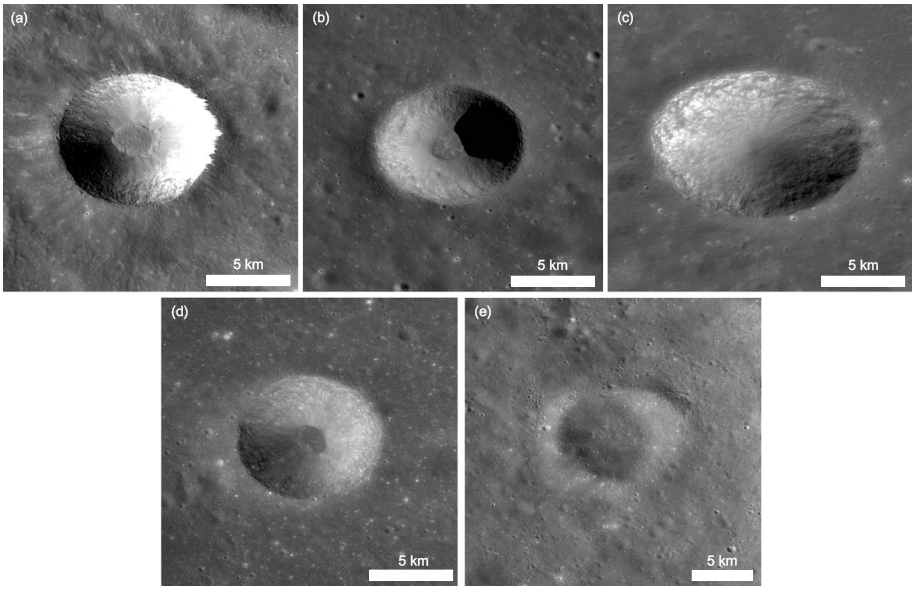

Figure 7. Kaguya Terrain Camera (TC) optical images for five selected impact craters in the highlands with different degradation states: (a) crater 1 (30.49°N, 84.02°E; 8.8 km), (b) crater 2 (37.92°S, 156.67°W; 6.9 km), (c) crater 3 (Shuckburgh E; 44.05°N, 57°E; 9.9 km), (d) crater 4 (30.94°N, 108.08°W; 7.9 km), and (e) crater 5 (39.55°N, 71.12°E; 7.0 km).

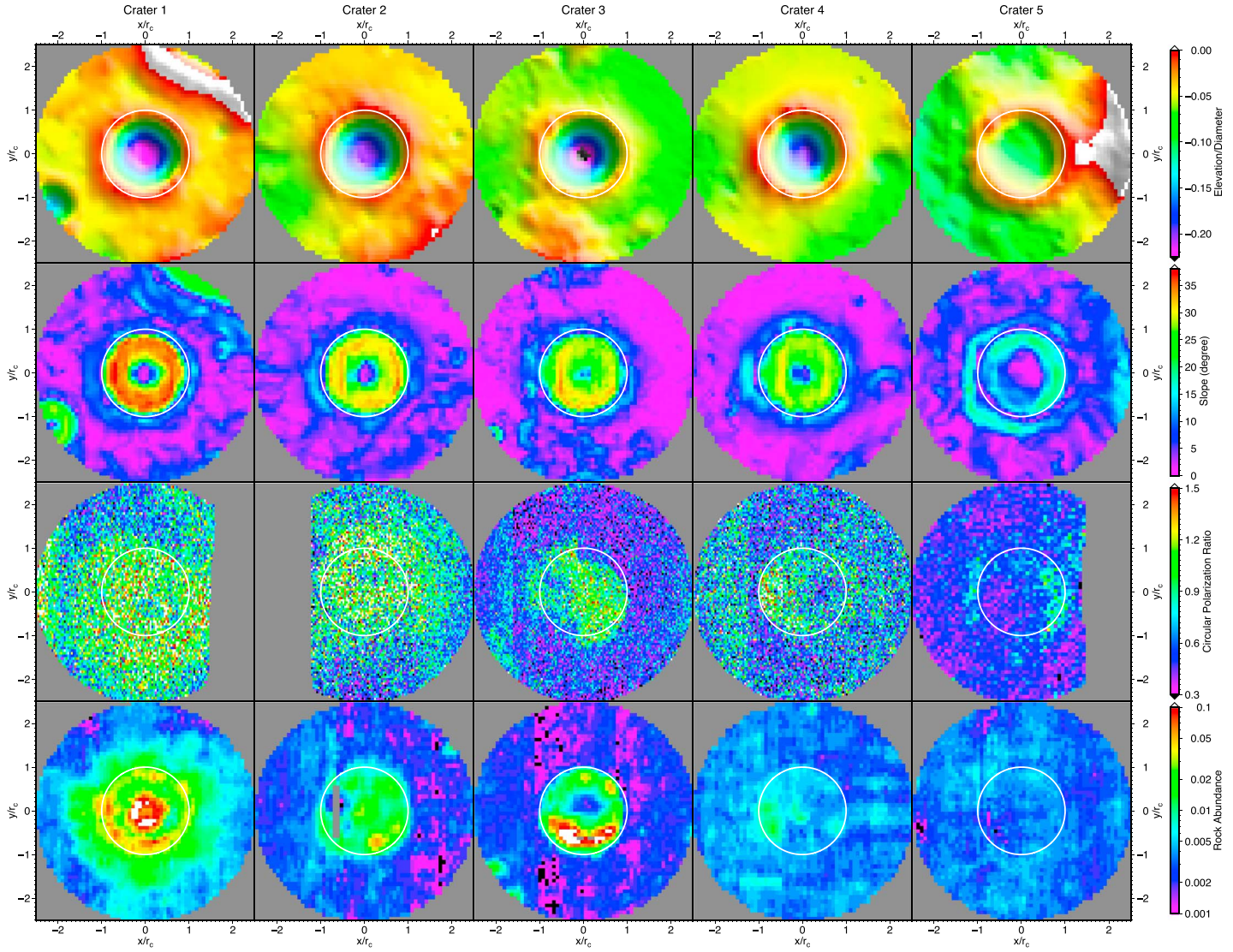

Figure 8. Normalized surface elevation (top row), slope (second row), CPR (third row) and RA (bottom row) for the selected five craters: crater 1 (the first column), crater 2 (the second column), crater 3 (Shuckburgh E) (the third column), crater 4 (the fourth column), and crater 5 (the fifth column).

ratio of crater 5 is much smaller. For each individual crater, the largest inner wall slope occurs about $0.5-0.9r_c$ from the crater center and this maximum slope decreases as the crater is degraded. For the two intermediate craters (3 and 4), interior CPR values are much higher than those of the corresponding exterior regions. For crater 4, the largest CPR occurs over the inner wall where surface slopes are the highest, which is consistent with the finding by Eke et al. (2014). Craters 3 and 4 both have a CPR that decreases rapidly with distance outside the crater rim. For the fresh crater 1, the exterior RA decreases gradually with distance, whereas RA decreases rapidly with distance for craters 2 and 3. RA values for craters 4 and 5 are roughly equal to the background value (~0.004–0.006) independent of cratercentric distance.

4. Discussion

In this section, we discuss potential factors for the high CPR values and the evolution of rocks associated with impact craters.

4.1. What is Responsible for the CPR Values?

The results in the previous section suggest that surface rocks as inferred from Diviner measurements are weathered away more rapidly than the surface and subsurface rocks that give rise to the high radar CPR. Both theoretical modeling and observations show that surface roughness and rocks either perched on the lunar

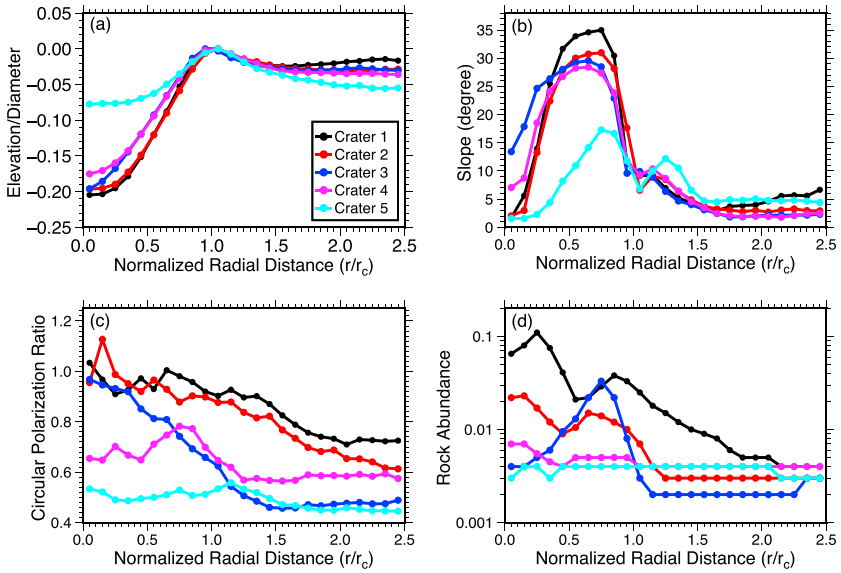

Figure 9. Radial profiles of the (a) normalized surface elevation, (b) slope, (c) CPR and (d) RA for the selected five craters.

surface or buried in the regolith are two major contributors to radar echoes from the lunar surface (e.g., Fa et al., 2011; Ghent et al., 2016). We now investigate the relative contributions to the CPR of surface and buried rocks in the context of the two-component mixture radar scattering model in Fa and Cai (2013). Surface or subsurface rocks with size from a few tenths to tens of radar wavelengths are good scatterers that can produce high radar echoes. In this model, radar CPR from a lunar surface consists of single scattering from a normal surface without rocks at meter scales and larger and double scattering from meter-scale rocks that can be either surficial or subsurface. The single scattering CPR depends mainly on surface roughness and rocks at wavelength scale and smaller (~cm) (Fa et al., 2011), whereas that from double scattering depends primarily on the abundance of rocks at meter scales and larger (Fa & Cai, 2013). Double scattering is modeled as two successive reflections from a dihedral structure that is much larger than the wavelength, which belongs to scattering in the optical region (compared to the Rayleigh and Mie regions). Scattering in the optical region occurs when a scatterer is ~10 wavelengths in size. This corresponds to a scale of ~1.3 m for Mini-RF S-band, which is roughly the same scale as that probed by the Diviner RA. Additionally, both the single and double scattering CPR vary with radar incidence angle, surface slope, and dielectric permittivity. The total CPR is simply the weighted sum of the two scattering terms, with a weighting factor of the surface/subsurface fraction of meter-scale rocks for double scattering and the fraction of normal surface for single scattering.

Requiring that both the Mini-RF and Diviner radiometer fractional coverages exceed 0.9 reduces our sample of 4,030 craters to 710 well-sampled impact craters. The dots in Figure 10 show the relations between CPR and RA for the well-sampled 710 impact craters. The two black curves in Figure 10 are the predicted CPR as a function of RA from the two-component mixture radar scattering model. In the model calculation, the single scattering CPR is chosen empirically as 0.5, and the double scattering CPR is chosen as 4, corresponding to a rock with a density of 3.15 g/cm^3 and a real part of the dielectric permittivity of 7.8 (Fa & Cai, 2013). As the single scattering CPR depends on surface roughness, centimeter-scale rocks, surface slope, and dielectric permittivity and the first three factors vary greatly across the lunar surface (Fa & Wieczorek, 2012; Rosenburg et al., 2011), the single scattering CPR should vary from place to place. By increasing (decreasing) the single scattering CPR value, the black curves in Figure 10 simply shift up (down). The grey regions in Figure 10 show the range of predicted CPR variation with the single scattering CPR changing from 0.3 to 0.7.

As can be seen, a significant number of craters fall into the model predicted grey regions, indicating that rocks and surface roughness could be the major contributors to their observed CPRs. However, there are craters with low surface RA but high CPR values (dots above the grey region), and there are also craters with high interior RA values but only intermediate CPR values (dots right of the grey region). Dots above the grey region indicate that either the surface or subsurface RA is underestimated. If subsurface rocks are considered in the model (Figure 10b), then the number of impact craters above the grey region decreases. For impact craters with

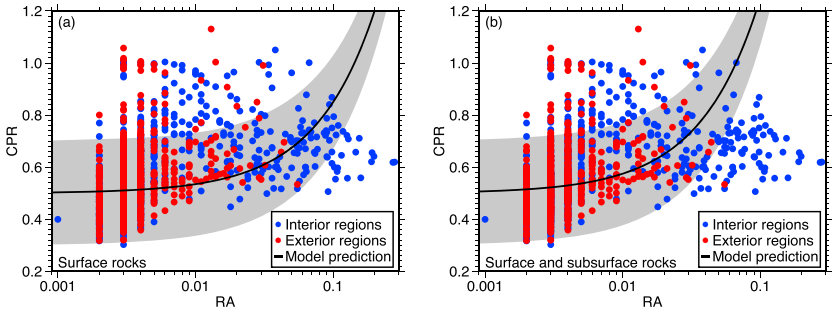

Figure 10. The relation between CPR and RA for 710 well-sampled impact craters (dots) and predictions from the two-component mixture radar scattering model in Fa and Cai (2013) (black lines): (a) no subsurface rocks are considered, and (b) both surface and subsurface rocks are included. In the model calculation, the single scattering CPR is chosen to be 0.5. The lower and upper boundaries of the grey regions correspond to a single scattering CPR of 0.3 and 0.7, respectively, and the double scattering CPR is chosen to be 4.0. CPR = circular polarization ratio; RA = rock abundance.

interior RA larger than 0.1, double scattering from only surface rocks can overestimate the CPR significantly. The discrepancy might result from differences in penetration depth and rock size between the S-band Mini-RF and the Diviner thermal radiometer. Diviner derived RA is for surface rocks at meter scales and larger, whereas the Mini-RF S-band is sensitive to rocks at scales of ~10 cm from the surface to a depth of 2–3 m. In addition, the double scattering CPR could vary across the surface, because it depends on dielectric permittivity and radar incidence angle and these two parameters could vary laterally.

4.2. Evolution of Rocks Associated with Impact Craters

The Diviner RA quantifies surface rocks at the meter scale and larger (Bandfield et al., 2011), whereas Mini-RF is sensitive to rocks down to the centimeter scale from the lunar surface to a depth of a few meters (typically ~1–3 m). Based on the evolutionary order of craters inferred from the morphological characteristics in Figure 7, the presence and evolution of meter-scale rocks in the vicinity of impact craters can be tracked in optical, infrared and radar images (Figures 8 and 9).

A newly formed crater possesses surface and subsurface rocks both inside and outside its rim, and therefore has a high CPR. Over time, both surface and subsurface rocks break down due to micrometeorite bombardment and other weathering processes. For fresh craters, the inner wall slope is generally much larger than the outer wall slope (e.g., crater 1 in Figures 8 and 9). As mass wasting depends largely on surface slope, surface rocks within crater rims are more readily replenished than those in the exterior regions. Consequently, the exterior RA decreases quickly to the background level, whereas the interior RA remains higher until mass wasting is no longer able to introduce new surface rocks at the same rate at which they are weathering away. Due to self-shielding by the lunar regolith, subsurface rocks break down more slowly than surface rocks. As radar waves are sensitive to subsurface rocks down to several meters, a low surface RA could coincide with a high CPR (e.g., the exterior of crater 2). Subsequently, subsurface rocks in the exterior region eventually break down while there are still surface rocks in the interior. This leads to craters like crater 3 with high interior RA and CPR and low exterior values, a defining characteristic for anomalous craters. When mass wasting becomes inefficient in replenishing the interior surface rocks, the interior RA will decrease while subsurface rocks keep the interior CPR high. Finally, the subsurface rocks in the interior either become covered by enough fine-grained regolith (at least 2–3 m) or break down and become much smaller than the radar wavelength (12.6 cm for the Mini-RF S-band), and the crater looks old in both the CPR and RA images (e.g., crater 5).

The question arises, how long does each crater evolution stage last? Equivalently, what are the survival times of meter-scale rocks at the surface and within the regolith based on radar and infrared observations? We selected 113 impact craters with known Absolute Model Ages (AMAs), 100 from Baldwin (1985) and the other 13 from Trang et al. (2015). Absolute model ages of these craters were estimated based on the density of craters formed on their rims and ejecta, and 92 craters have a relative uncertainty in age <30%. In total, there are 104 craters in the RA map with interior and exterior RA coverage ≥90%, and 62 craters in the CPR map with interior and exterior CPR coverage ≥50%. Figure 11 shows the surface RA and radar CPR values as functions of crater age for both the interior and exterior regions. We used an exponential decay function to fit both CPR

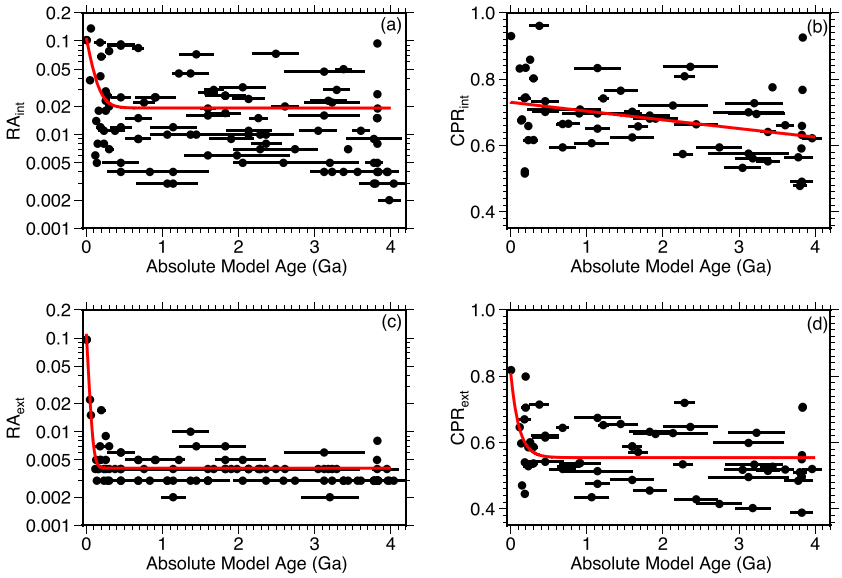

Figure 11. Interior (top) and exterior (bottom) rock abundance (left) and CPR (right) as a function of age for 113 selected craters. Error bars show the uncertainties in the absolute model ages.

and RA as a function of crater age, t, via

$$F(t) = F_0 \exp(-kt) + F_b \quad , \tag{1}$$

where F represents RA or CPR, $F_0 + F_b$ is the initial value for fresh craters, F_b is the background value, and k is a constant indicating how rapidly $F(t)$ decays.

Table 2 shows the best-fitting coefficients for the interior and exterior CPR and RA and their uncertainties. The interior CPR decays so slowly, presumably as a result of mass wasting on the steep inner slopes, that the best-fitting F_0 and F_b values for this case are individually poorly constrained. These parameters are highly anticorrelated such that a larger value of one implies a lower value of the other. However, the relative decay timescales for all quantities can reliably be compared. k values for CPR are much smaller than the corresponding ones for RA, indicating that CPR decays more slowly than RA. This is because radar CPR is sensitive to both surface and subsurface rocks whereas Diviner RA is only for surface rocks. For the exterior region of an impact crater, the surface slope is generally small, and hence mass wasting does not significantly refresh surface rocks. Therefore, the rate at which exterior surface rocks break down should be representative of that for a normal flat surface. From the fitting of the exterior RA, the median survival time of meter-scale rocks is about 20 Ma, and the 99% survival time (99% of meter-scale rocks have broken down) is about 120 Ma. Basilevsky et al. (2013) counted >1,600 boulders at least 2 m in diameter on the rims of 12 lunar craters (150–950 m in diameter) with known ages and found that the median survival time of meter-scale surface rocks is about 40–80 Ma and that the 99% survival time is about 150–300 Ma. Our times are generally smaller than those in Basilevsky et al. (2013), which might result from the difference in the size of surface rocks in the two studies. Another reason could be that Basilevsky et al. (2013) investigated craters smaller than 1 km, whereas the minimum crater in our study is 2.5 km in diameter. Perhaps mantling of rocks by a surface regolith layer could act differently in different sized craters.

Table 2
Coefficients in the Fitting of the CPR and RA Decay with Age

F	F_0	k/(Ga^{-1})	F_b
RA_{int}	**0.09** (0.05, 0.12)	**12.0** (4.4, 19.5)	**0.02** (0.01 0.02)
RA_{ext}	**0.11** (0.10, 0.11)	**37.6** (33.9, 41.4)	**0.0041** (0.0037, 0.0045)
CPR_{int}	**1.96** (−212.8, 216.7)	**0.014** (−1.5, 1.6)	**-1.23** (−216, 213.6)
CPR_{ext}	**0.25** (0.07, 0.44)	**9.3** (1.3, 17.3)	**0.55** (0.5, 0.6)

Note. Numbers in bold are the best-fit coefficients whereas those in brackets correspond to the 95% confidence intervals.

We also examined the impact craters in Trang et al. (2015) and found that the youngest crater (Hainzel L) with low interior and exterior CPR and no surface rocks is ~3.8 Ga old. This may imply that craters could spend up to a few billion years in the CPR-anomalous phase, and that this represents an upper limit on the survival time of subsurface rocks.

5. Conclusions

In this study, we constructed two controlled orthorectified global Mini-RF mosaics, and systematically investigated the correlations between radar CPR, surface slope, RA, and depth/diameter ratio for >4,000 impact craters. Our results imply the following:

1. CPR-anomalous craters are distributed relatively uniformly across the lunar surface. Once the Mini-RF spatially varying sampling is accounted for, there is no evidence to support the hypothesis that polar CPR-anomalous craters are overabundant. Hence, Mini-RF CPR data do not provide evidence to support the existence of a large quantity of pure water ice over the lunar poles.
2. Most CPR-anomalous craters are relatively young with large depth/diameter ratios, indicating that they are just at an intermediate stage of normal crater evolution.
3. Comparison between a two-component mixture radar scattering model and the observations show that the model can match the observations for a significant number of craters, indicating that rocks and surface roughness are the major contributors to the observed CPR values. There are discrepancies for a few craters, but these may be explained by differences in the penetration depth and rock size being probed by Mini-RF and the Diviner radiometer.
4. Preliminary results show that crater exteriors spend up to ~120 Ma with Diviner RA≥0.01 and ~3 Ga in the CPR-anomalous phase.

Our results show that the existence and spatial distribution of CPR-anomalous craters on the Moon do not indicate the presence of large quantities of pure water ice in the polar regions. To find convincing evidence for highly concentrated deposits of water ice using radar CPR, one would need to exclude alternative explanations as the cause for such CPR signals. With several planned missions focusing on the polar regions (e.g., NASA's Lunar Resource Prospector, China's Chang'E-P1) in the next 10 years (e.g., Lawrence, 2017), more direct evidence for water ice deposits should be forthcoming, allowing their locations and amounts to be quantified.

Even though we find that CPR-anomalous craters provide no significant new constraints on polar water ice deposits, such craters form part of a sequence that can help us to understand the formation and evolution of impact craters and their ejecta. In future, if the ages of individual craters can be estimated with higher accuracy, then the duration of each evolutionary stage can be more tightly constrained. In addition, the behavior of impact craters <1 km in diameter would be another interesting future topic for providing insight into the lunar regolith.

Acknowledgments
We thank Catherine Neish and Randy Kirk for helpful guidance concerning Mini-RF data reduction. The authors gratefully acknowledge NASA PDS Geosciences Node for providing Mini-RF, Diviner RA, and LOLA topography data. Figures were created using the Generic Mapping Tools of Wessel and Smith (1991). This work was supported partly by the National Natural Science Foundation of China (11573005 and 41490634), the Science and Technology Development Fund of Macau (043/2016/A2 and 119/2017/A3), and the Open Fund of the Key Laboratory for Information Science of Electromagnetic Waves (EMW201503). W. Fa thanks the COFUND Senior Research Fellowship by the Institute of Advanced Study, Durham University. V. R. Eke was supported by the Science and Technology Facilities Council (STFC) through grant ST/P000541/1. Mini-RF data processing and crater finding work used the DiRAC Data Centric system at Durham University, operated by the Institute for Computational Cosmology on behalf of the STFC DiRAC HPC Facility (http://www.dirac.ac.uk). This equipment was funded by BIS National E-infrastructure capital grant ST/K00042X/1, STFC capital grant ST/H008519/1, and STFC DiRAC Operations grant ST/K003267/1 and Durham University. DiRAC is part of the National E-Infrastructure. The Mini-RF global mosaics are available at: http://astro.dur.ac.uk/~vreke/mini/. This is PKU PRSL contribution 10.

References

Arnold, J. R. (1979). Ice in the lunar polar regions. *Journal of Geophysical Research*, *84*(B10), 5659–5668. https://doi.org/10.1029/JB084iB10p05659

Baldwin, R. B. (1985). Relative and absolute ages of individual craters and the rate of infalls on the moon in the post-imbrium period. *Icarus*, *61*(1), 63–91.

Bandfield, J. L., Ghent, R. R., Vasavada, A. R., Paige, D. A., Lawrence, S. J., & Robinson, M. S. (2011). Lunar surface rock abundance and regolith fines temperatures derived from LRO diviner radiometer data. *Journal of Geophysical Research*, *116*, E00H02. https://doi.org/10.1029/2011JE003866

Bandfield, J. L., Song, E., Hayne, P. O., Brand, B. D., Ghent, R. R., Vasavada, A. R., & Paige, D. A. (2014). Lunar cold spots: Granular flow features and extensive insulating materials surrounding young craters. *Icarus*, *231*, 221–231.

Basilevsky, A. T., Head, J. W., & Horz, F. (2013). Survival times of meter-sized boulders on the surface of the moon. *Planetary and Space Science*, *89*, 118–126.

Cahill, J. T., Thomson, B., Patterson, G. W., Bussey, D. B. J., Neish, C. D., Lopez, N. R., et al. (2014). The miniature radio frequency instrument's (mini-RF) global observations of Earth's Moon. *Icarus*, *243*, 173–190.

Campbell, B. A. (2002). *Radar Remote Sensing of Planetary Surfaces*. New York: Cambridge University Press.

Carter, L. M., Campbell, D. B., & Campbell, B. A. (2011). Geologic studies of planetary surfaces using radar polarimetric imaging. *Proceedings of the IEEE*, *99*(5), 770–782.

Colaprete, A., Schultz, P., Heldmann, J., Wooden, D., Shirley, M., Ennico, K., et al. (2010). Detection of water in the LCROSS ejecta plume. *Science*, *330*(6003), 463–468.

Eke, V. R., Bartram, S. A., Lane, D. A., Smith, D., & Teodoro, L. F. (2014). Lunar polar craters—Icy, rough or just sloping? *Icarus*, *241*, 66–78.

Eke, V. R., Lawrence, D. J., & Teodoro, L. F. (2017). How thick are Mercury's polar water ice deposits? *Icarus*, *284*, 407–415.

Eke, V. R., Teodoro, L. F. A., & Elphic, R. C. (2009). The spatial distribution of polar hydrogen deposits on the Moon. *Icarus*, *200*, 12–18.

Fa, W., & Cai, Y. (2013). Circular polarization ratio characteristics of impact craters from mini-RF observations and implications for ice detection at the polar regions of the Moon. *Journal of Geophysical Research: Planets*, *118*, 1582–1608. https://doi.org/10.1002/jgre.20110

Fa, W., & Wieczorek, M. A. (2012). Regolith thickness over the lunar nearside: Results from Earth-based 70-cm Arecibo radar observations. *Icarus*, *218*(2), 771–787.

Fa, W., Wieczorek, M. A., & Heggy, E. (2011). Modeling polarimetric radar scattering from the lunar surface: Study on the effect of physical properties of the regolith layer. *Journal of Geophysical Research*, *116*, E03005. https://doi.org/10.1029/2010JE003649

Fassett, C. I., & Thomson, B. J. (2014). Crater degradation on the lunar maria: Topographic diffusion and the rate of erosion on the Moon. *Journal of Geophysical Research: Planets*, *119*, 2255–2271. https://doi.org/10.1002/2014JE004698

Ghent, R., Carter, L., Bandfield, J., Udovicic, C. T., & Campbell, B. (2016). Lunar crater ejecta: Physical properties revealed by radar and thermal infrared observations. *Icarus*, *273*, 182–195.

Gong, X., & Jin, Y.-Q. (2013). Diurnal change of MW and IR thermal emissions from lunar craters with relevance to rock abundance. *Acta Astronautica*, *86*, 237–246. https://doi.org/10.1016/j.actaastro.2013.01.020

Hapke, B. (1990). Coherent backscatter and the radar characteristics of outer planet satellites. *Icarus*, *88*(2), 407–417.

Head, J. W., Fassett, C. I., Kadish, S. J., Smith, D. E., Zuber, M. T., Neumann, G. A., & Mazarico, E. (2010). Global distribution of large lunar craters: Implications for resurfacing and impactor populations. *Science*, *329*(5998), 1504–1507.

Kirk, R., Cook, D., Howington-Kraus, E., Barrett, J., Becker, T., Neish, C., et al. (2010). Radargrammetry with Chandrayaan-1 and LRO Mini-RF images of the Moon. ISPRS Commission IV, WG IV/7.

Koeber, S. D., Robinson, M. S., & Speyerer, E. J. (2014). LROC observations of permanently shadowed regions on the Moon. In *The 45Th Lunar and Planetary Science Conference*, pp. 2811.

Laneuville, M., Wieczorek, M. A., Breuer, D., & Tosi, N. (2013). Asymmetric thermal evolution of the Moon. *Journal of Geophysical Research: Planets*, *118*, 1435–1452. https://doi.org/10.1002/jgre.20103

Lawrence, D. J. (2017). A tale of two poles: Toward understanding the presence, distribution, and origin of volatiles at the polar regions of the moon and mercury. *Journal of Geophysical Research: Planets*, *122*, 21–52. https://doi.org/10.1002/2016JE005167

Lawrence, D. J., Hurley, D. M., Feldman, W. C., Elphic, R. C., Maurice, S., Miller, R. S., & Prettyman, T. H. (2011). Sensitivity of orbital neutron measurements to the thickness and abundance of surficial lunar water. *Journal of Geophysical Research*, *116*, E01002. https://doi.org/10.1029/2010JE003678

Le Feuvre, M., & Wieczorek, M. A. (2011). Nonuniform cratering of the Moon and a revised crater chronology of the inner Solar System. *Icarus*, *214*(1), 1–20.

Li, S., & Milliken, R. E. (2017). Water on the surface of the Moon as seen by the Moon Mineralogy Mapper: Distribution, abundance, and origins. *Science Advances*, *3*(9), e1701471. https://doi.org/10.1126/sciadv.1701471

Lucey, P. G. (2009). A lunar waterworld. *Science*, *326*(5952), 531–532.

Lucey, P. G., Neumann, G. A., Riner, M. A., Mazarico, E., Smith, D. E., Zuber, M. T., et al. (2014). The global albedo of the Moon at 1064 nm from LOLA. *Journal of Geophysical Research: Planets*, *119*, 1665–1679. https://doi.org/10.1002/2013JE004592

Melosh, H. J. (1989). *Impact Cratering: A Geologic Process*. New York: Oxford University Press.

Melosh, H. J. (2011). *Planetary Surface Processes*. Cambridge: Cambridge University Press.

Mitchell, J., Lawrence, S., Robinson, M., Speyerer, E., & Denevi, B. (2017). Using complementary remote sensing techniques to assess the presence of volatiles at the lunar north pole. *Planetary and Space Science*. https://doi.org/10.1016/j.pss.2017.07.015

Morota, T., Haruyama, J., Ohtake, M., Matsunaga, T., Honda, C., Yokota, Y., et al. (2011). Timing and characteristics of the latest mare eruption on the Moon. *Earth and Planetary Science Letters*, *302*(3–4), 255–266.

Neish, C. D., Bussey, D. B. J., Spudis, P., Marshall, W., Thomson, B. J., Patterson, G. W., & Carter, L. M. (2011). The nature of lunar volatiles as revealed by mini-RF observations of the LCROSS impact site. *Journal of Geophysical Research*, *116*, E01005. https://doi.org/10.1029/2010JE003647

Nozette, S., Spudis, P., Bussey, B., Jensen, R., Raney, K., Winters, H., et al. (2010). The Lunar Reconnaissance Orbiter Miniature Radio Frequency (Mini-RF) technology demonstration. *Space Science Reviews*, *150*(1–4), 285–302.

Paige, D. A., Siegler, M. A., Zhang, J. A., Hayne, P. O., Foote, E. J., Bennett, K. A., et al. (2010). Diviner Lunar Radiometer observations of cold traps in the Moon's south polar region. *Science*, *330*(6003), 479–482.

Patterson, G., Stickle, A., Turner, F., Jensen, J., Bussey, D., Spudis, P., et al. (2017). Bistatic radar observations of the Moon using Mini-RF on LRO and the Arecibo Observatory. *Icarus*, *283*, 2–19.

Peters, K. J. (1992). Coherent-backscatter effect: A vector formulation accounting for polarization and absorption effects and small or large scatterers. *Physical Review B*, *46*, 801–812.

Pieters, C. M., Goswami, J. N., Clark, R. N., Annadurai, M., Boardman, J., Buratti, B., et al. (2009). Character and spatial distribution of OH/H_2O on the surface of the Moon Seen by M^3 on Chandrayaan-1. *Science*, *326*(5952), 568–572.

Pohn, H. A., & Offield, T. W. (1970). Lunar crater morphology and relative age determination of lunar geologic units—Part 1 Classification (*Technical report*). Flagstaff, AZ: U. S. Geological Survey.

Raney, R., Spudis, P., Bussey, B., Crusan, J., Jensen, J., Marinelli, W., et al. (2011). The lunar Mini-RF radars: Hybrid polarimetric architecture and initial results. *Proceedings of the IEEE*, *99*(5), 808–823.

Rosenburg, M. A., Aharonson, O., Head, J. W., Kreslavsky, M. A., Mazarico, E., Neumann, G. A., et al. (2011). Global surface slopes and roughness of the Moon from the Lunar Orbiter Laser Altimeter. *Journal of Geophysical Research*, *116*, E02001. https://doi.org/10.1029/2010JE003716

Ross, H. P. (1968). A simplified mathematical model for lunar crater erosion. *Journal of Geophysical Research*, *73*(4), 1343–1354. https://doi.org/10.1029/JB073i004p01343

Salamunićcar, G., Lončarić, S., Grumpe, A., & Wöhler, C. (2014). Hybrid method for crater detection based on topography reconstruction from optical images and the new LU78287GT catalogue of lunar impact craters. *Advances in Space Research*, *53*(12), 1783–1797.

Speyerer, E. J., Povilaitis, R. Z., Robinson, M. S., Thomas, P. C., & Wagner, R. V. (2016). Quantifying crater production and regolith overturn on the moon with temporal imaging. *Nature*, *538*(7624), 215–218.

Spudis, P. D., Bussey, D. B. J., Baloga, S. M., Butler, B. J., Carl, D., Carter, L. M., et al. (2010). Initial results for the north pole of the Moon from mini-SAR, Chandrayaan-1 mission. *Geophysical Research Letters*, *37*, L06204. https://doi.org/10.1029/2009GL042259

Spudis, P. D., Bussey, D. B. J., Baloga, S. M., Cahill, J. T. S., Glaze, L. S., Patterson, G. W., et al. (2013). Evidence for water ice on the Moon: Results for anomalous polar craters from the LRO mini-RF imaging radar. *Journal of Geophysical Research: Planets*, *118*, 2016–2029. https://doi.org/10.1002/jgre.20156

Thompson, T. W., Ustinov, E. A., & Heggy, E. (2011). Modeling radar scattering from icy lunar regoliths at 13 cm and 4 cm wavelengths. *Journal of Geophysical Research*, *116*, E01006. https://doi.org/10.1029/2009JE003368

Thomson, B. J., Bussey, D. B. J., Neish, C. D., Cahill, J. T. S., Heggy, E., Kirk, R. L., et al. (2012). An upper limit for ice in Shackleton crater as revealed by LRO mini-RF orbital radar. *Geophysical Research Letters*, *39*, L14201. https://doi.org/10.1029/2012GL052119

Trang, D., Gillis-Davis, J. J., & Boyce, J. M. (2015). Absolute model ages from lunar crater morphology. *Journal of Geophysical Research: Planets*, *120*, 725–738. https://doi.org/10.1002/2014JE004639

Wessel, P., & Smith, W. H. F. (1991). Free software helps map and display data. *EOS Transactions American Geophysical Union*, *72*(41), 441–446.

Williams, J.-P., Paige, D., Greenhagen, B., & Sefton-Nash, E. (2017). The global surface temperatures of the Moon as measured by the Diviner Lunar Radiometer Experiment. *Icarus*, *283*, 300–325.

Xiao, Z., Zeng, Z., Ding, N., & Molaro, J. (2013). Mass wasting features on the Moon—How active is the lunar surface? *Earth and Planetary Science Letters*, *376*, 1–11.

Erratum

In the originally published version of this manuscript, the supplementary spreadsheet containing the crater data was mistakenly omitted. This error has since been corrected and the file has been added. This version may be considered the authoritative version of record.